

Received 27 October 2023, accepted 29 November 2023, date of publication 5 December 2023,  
date of current version 12 December 2023.

Digital Object Identifier 10.1109/ACCESS.2023.3339549

## RESEARCH ARTICLE

# A Multi-Stage Hybrid Open-Circuit Fault Diagnosis Approach for Three-Phase VSI-Fed PMSM Drive Systems

FAZEL MOHAMMADI<sup>1</sup>, (Senior Member, IEEE),  
AND MEHRDAD SAIF<sup>2</sup>, (Senior Member, IEEE)

<sup>1</sup>Electrical and Computer Engineering and Computer Science Department, University of New Haven, West Haven, CT 06516, USA

<sup>2</sup>Department of Electrical and Computer Engineering, University of Windsor, Windsor, ON N9B 3P4, Canada

Corresponding author: Fazel Mohammadi (fmohammadi@newhaven.edu)

**ABSTRACT** The performance of Hybrid Electric Vehicles (HEVs), especially in series architecture, is highly dependent on the reliability of electric drive-motor systems. Any failure in power semiconductor devices, such as Insulated-Gate Bipolar Transistors (IGBTs), used in three-phase Voltage Source Inverters (VSIs) for Permanent Magnet Synchronous Motor (PMSM) drive systems, causes a reduction in the reliability and leads to unscheduled maintenance of HEVs. This paper aims to present a three-stage combined model-based and data-driven fault diagnosis approach, the so-called hybrid fault diagnosis approach, to detect, locate, and clear open-circuit faults in IGBTs used in VSI-fed PMSM drive systems in HEVs. Field-Oriented Control (FOC), which is a model-based technique, is used to control the electric drive-motor system. The proposed method, which is based on phase voltage analysis, estimates the current in each phase of VSI using the normal operating conditions dataset to detect open-circuit faults in IGBTs. Once a fault is detected, it is located using the faulty conditions dataset and an online data-driven approach, called the Modified Multi-Class Support Vector Machine (MMC-SVM) algorithm. Thereafter, the faulty IGBT is bypassed by closing the corresponding backup switch, ensuring the continuous operation of the electric drive-motor system. The proposed method can accurately and quickly detect, locate, and clear open-circuit faults in IGBTs without the need for additional sensors. Additionally, it demonstrates robustness against back-to-back and simultaneous faults in IGBTs used in VSI-fed PMSM drive systems in HEVs.

**INDEX TERMS** Fault diagnosis, hybrid electric vehicle (HEV), insulated-gate bipolar transistor (IGBT), open-circuit fault, permanent magnet synchronous motor (PMSM), voltage source inverter (VSI).

## I. INTRODUCTION

In the past few decades, environmental concerns for fossil fuel-based transportation infrastructure have caused tremendous interest in more electric transportation infrastructure. Unlike Internal Combustion Engine (ICE)-based vehicles that mainly rely on petroleum, a significant portion of consumed power by Hybrid Electric Vehicles (HEVs) is from different energy sources, such as batteries, fuel cells, supercapacitors, etc., along with using electric drive-motor systems [1], [2]. Despite the benefits of HEVs, such as less greenhouse

gas emissions, less noise pollution, and higher energy efficiency, failures in their main components, particularly the Permanent Magnet Synchronous Motor (PMSM), Voltage Source Inverter (VSI), Energy Storage System (ESS), etc., incur heavy expenses and may put the safety of HEVs in danger [3], [4].

Early-stage failures can be due to overvoltage, overcurrent, or overheating in components such as batteries and/or electric drive-motor systems, and it may be more difficult to diagnose failures if other factors, such as noise, vibration, electromagnetic field, frequency, torque, etc., are involved [5], [6]. Hence, to minimize the computational burden and fast recovery of the HEV, it is crucial to find

The associate editor coordinating the review of this manuscript and approving it for publication was Derek Abbott<sup>1</sup>.

the source of failure. In particular, the major faults of ESSs, specifically batteries, in HEVs can be due to (1) over-charge/discharge, (2) overheating/undercooling, (3) short circuit/open-circuit of internal cells, and (4) incorrect state estimation [7], [8], [9]. In addition, (1) abnormal connection of stator windings, (2) short circuit/open-circuit of stator windings, (3) short circuit of rotor windings, (4) broken rotor bars, (5) eccentricity-related faults, and (6) bearing faults are the main faults of electric motors, particularly PMSMs, in HEVs [11], [12]. Moreover, (1) short circuit/open-circuit faults of switches and (2) intermittent gate-misfiring faults are the dominant faults in electric drive systems, mainly VSIs, in HEVs [13], [14].

The risk of failure of power semiconductor devices, particularly Insulated-Gate Bipolar Transistor Bipolar Transistors (IGBTs), used in VSI-fed PMSM drive systems is high. This is due to the fact that such devices are exposed to thermal stress and various harsh environmental and operating conditions. Fault diagnosis of power semiconductor devices has been investigated in many research studies. Short circuit faults in power semiconductor devices occur rapidly and can cause potential destruction. Using hardware protection systems, such faults can be cleared in electric drive systems. A summary of hardware protection systems for short circuit faults is provided in [15]. The impacts of open-circuit faults in power semiconductor devices can potentially lead to VSIs malfunctioning, and consequently their outage and great economic loss [16]. In this regard, various fault-tolerant control approaches are presented in the literature [17], [18], [19], [20], [21] aiming at fast fault diagnosis.

Open-circuit fault diagnosis approaches can be either current-based or voltage-based methods. In current-based approaches, (1) there is no need for additional sensors, and (2) by employing the existing current sensors in the control loop, current can be measured to diagnose the fault. The presented current-based fault diagnosis methods in the literature can be classified into two major categories: current-signal-based and current-observer-based approaches. The current-signal-based approaches are prone to generating false signals under different transient conditions of electric drive systems and require a longer time to accurately diagnose the fault. In particular, in [22], the characteristics of the current vector trajectory under various faulty conditions are investigated, and the slope of the current vector trajectory is used to diagnose faults. The average current Park's vector approach is presented in [23] to diagnose VSI faults in variable-speed AC electric drive systems. The major drawback of the presented methods in [22] and [23] is their inability to accurately diagnose faults when the load current is small. To mitigate the impact of the load current, normalized current-based approaches, such as normalized current Direct Current (DC) components approach [24], the absolute value of the normalized current and the current zero-crossing detection method [25], and the average value of the normalized line-to-line current [26] are investigated.

On the contrary, current-observer-based approaches require the residual signals, which are defined as the error between the measured outputs of the system and the estimated outputs provided by the observer [27], [28]. In [29], a nonlinear Proportional-Integral (PI) observer is investigated to the DC component of the fault profiles, and a directional residual evaluation is presented to isolate faults. A model-based approach using phasor representation of the residual vector is presented in [30] to detect and isolate faults in electric drive systems. An open-circuit fault diagnosis method for electric drive systems based on the current residual vector is presented in [31]. In [32], the zero voltage vector sampling fault diagnosis method is presented using the single DC-link current sensor. The concept of allelic points and their functions are presented in [33] to analyze the VSI-fed vector-controlled electric drives under normal operating conditions and faulty conditions. The performance of the current-based methods is highly dependent on the accuracy of model parameters, and they also, require high computation time for fault diagnosis.

Unlike current-based methods, voltage-based approaches are faster in terms of diagnosis speed while there is a need for additional voltage sensors and/or hardware in real-world applications. Particularly, in [34], an open-circuit fault detection approach based on the voltage model analysis is presented where the voltage measurements are compared with their corresponding reference values. In [35], a fast fault detection method with the aim of minimizing the time interval between the fault occurrence and its diagnosis using a Field-Programmable Gate Array (FPGA) is investigated. The presented method requires complex hardware and high implementation costs. A sectoral diagnosis method using voltage measurements is presented in [36] to diagnose open-circuit faults of inverter-fed PMSM drives. The presented method in [36] utilizes a separate residual between reference and measured pole voltage values for each of the switches instead of direct use of the instantaneous difference to improve the robustness of the presented method against variations of AC voltage within one cycle of rotation. Additionally, in [37], an indirect voltage measurement method using high-speed diagnostic photocouplers is investigated to deal with the complexity of the fault diagnosis circuit. A Model Reference Adaptive System (MRAS)-based voltage distortion observer is presented in [38] to diagnose open-circuit faults in VSI for PMSM drive. The complexity of design, additional sensor requirement to measure VSI pole voltage, machine phase voltage, system line voltage, and/or machine neutral point voltage, and the cost of implementation are the major challenges with voltage-based approaches to diagnose open-circuit faults in VSI-fed PMSM drives.

In addition to model-dependent methods, some data-driven techniques, such as Neural Networks (NN) [39], Artificial Neural Networks (ANN) [40], [41], Bayesian networks [42], Fuzzy Logic (FL) [43], [44], Wavelet Transform (WT) analysis [45], and hybrid Support Vector Machine (SVM) and WT analysis [46], [47], are investigated to diagnose

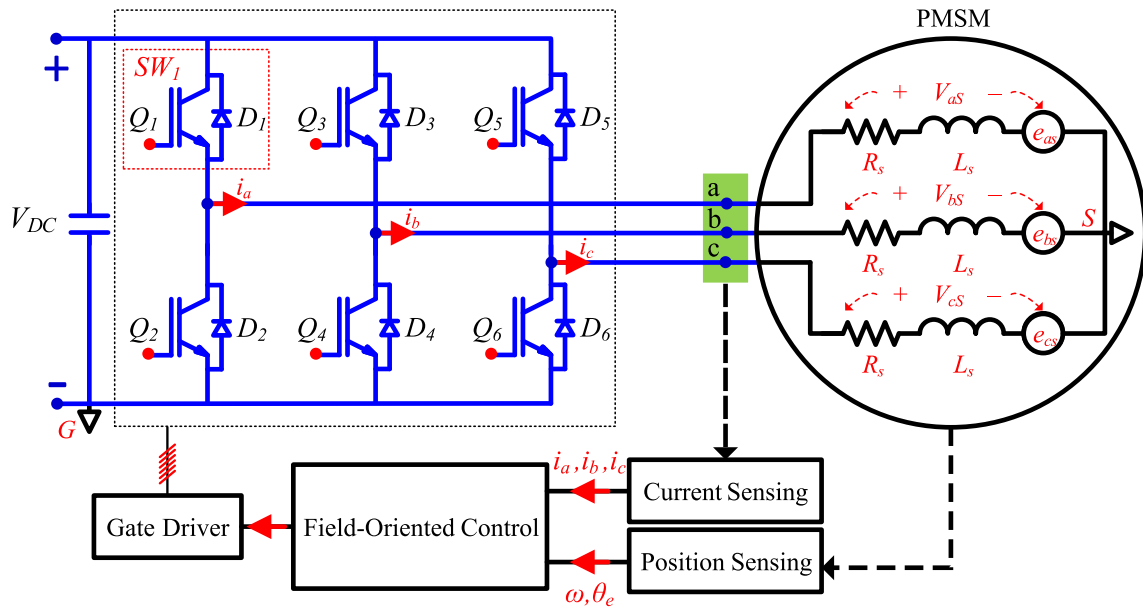


FIGURE 1. The structure of a three-phase VSI-fed PMSM drive system.

open-circuit faults in VSI-fed PMSM drives. However, challenges associated with such techniques are the complexity in design and implementation, high computational burden, and robustness against external factors, such as noise.

This paper presents a fast online (real-time) fault diagnosis approach for open-circuit faults in IGBTs used in VSI-fed PMSM drive systems in HEVs. The proposed approach, which is a three-stage combined model-based and data-driven fault diagnosis approach, is capable of quickly detecting open-circuit faults in IGBTs and accurately obtaining diagnosis results to locate and clear such faults without the need for additional sensors. The proposed method analyzes the three-phase voltage signals under normal operating conditions and various faulty conditions, and accordingly, estimates the current in each phase using the normal operating conditions dataset to detect open-circuit faults. Using the faulty conditions dataset and applying a data-driven approach, called the Modified Multi-Class Support Vector Machine (MMC-SVM) algorithm with Radial Basis Function (RBF) kernel function, such faults can be located. Once a fault is detected and located, the proposed method bypasses such faults by sending the closing command to the corresponding backup switches and ensures the continuous operation of the electric drive-motor system. Various scenarios, including single, multiple, and simultaneous faults in IGBTs, and also changes in PMSM operating conditions, are considered to assess and verify the performance of the proposed method. Considering the characteristics of the proposed open-circuit fault diagnosis method, it can be embedded in the existing VSI-fed PMSM drive systems without extensive changes.

The rest of this paper is organized as follows. A thorough analysis of IGBT open-circuit faults in VSI-fed PMSM drive systems is performed in Section II. Section III presents

the proposed open-circuit fault diagnosis approach in detail. Results and discussion are provided in Section IV. Finally, Section V concludes this paper.

## II. ANALYSIS OF IGBT OPEN-CIRCUIT FAULTS IN VSI-FED PMSM DRIVE SYSTEMS

Figure 1 shows the structure of a three-phase VSI-fed PMSM drive system using Field-Oriented Control (FOC). The main role of the control section is to generate the gate pulses based on the expected voltage and feed them into the VSI. The output of the VSI is applied to the PMSM windings to generate continuous current. Each leg of the VSI consists of two IGBTs, and  $i^{th}$  IGBT is indicated by  $SW_i$ , which comprises  $Q_i$  and  $D_i$ . Each  $SW$  is controlled by the gate driver, which sends gate pulses to the corresponding IGBTs. Using a three-phase current sensor, the current in each phase, i.e.,  $i_a$ ,  $i_b$ , and  $i_c$ , can be measured. In addition,  $\theta_e$  and  $\omega$ , which are the rotor electrical angle and the measured angular velocity, respectively, can be determined using position sensor signal processing. In Figure 1,  $V_{DC}$  represents the DC voltage across the DC-link capacitor.

### A. PHASE VOLTAGE ANALYSIS UNDER NORMAL OPERATING CONDITIONS

In the VSI-fed PMSM drive system, switching states determine the current flow under different conditions, and accordingly, the output voltage of the VSI varies. Hence, it is necessary to investigate the output voltage under different switching states, and for each  $SW$ , the switching state can be either ON or OFF. In this case, Table 1 illustrates the relationship between switching states of IGBTs and winding-to-ground voltage of phases  $a$ ,  $b$ , and  $c$ , respectively, i.e.,  $V_{aG}^N$ ,  $V_{bG}^N$ , and  $V_{cG}^N$ , under normal operating conditions.

**TABLE 1.** The relationship between switching states and the winding-to-ground voltage under normal operating conditions.

State Number	SW <sub>1</sub>	SW <sub>2</sub>	SW <sub>3</sub>	SW <sub>4</sub>	SW <sub>5</sub>	SW <sub>6</sub>	V <sub>aG</sub> <sup>N</sup>	V <sub>bG</sub> <sup>N</sup>	V <sub>cG</sub> <sup>N</sup>
0	OFF	ON	OFF	ON	OFF	ON	0	0	0
1	OFF	ON	OFF	ON	ON	OFF	0	0	V <sub>DC</sub>
2	OFF	ON	ON	OFF	OFF	ON	0	V <sub>DC</sub>	0
3	OFF	ON	ON	OFF	ON	OFF	0	V <sub>DC</sub>	V <sub>DC</sub>
4	ON	OFF	OFF	ON	OFF	ON	V <sub>DC</sub>	0	0
5	ON	OFF	OFF	ON	ON	OFF	V <sub>DC</sub>	0	V <sub>DC</sub>
6	ON	OFF	ON	OFF	OFF	ON	V <sub>DC</sub>	V <sub>DC</sub>	0
7	ON	OFF	ON	OFF	ON	OFF	V <sub>DC</sub>	V <sub>DC</sub>	V <sub>DC</sub>

In a three-phase PMSM with star-connected winding, the following condition is satisfied by Kirchhoff's law:

$$i_a + i_b + i_c = 0 \tag{1}$$

In addition, considering the sinusoidal air-gap magnetic flux distribution, the summation of phase voltage is equal to zero. Hence, based on Equation (1), the following equation for the PMSM can be written:

$$V_{aS} + V_{bS} + V_{cS} = R_s(i_a + i_b + i_c) + L_s \frac{d}{dt}(i_a + i_b + i_c) + (e_{aS} + e_{bS} + e_{cS}) = 0 \tag{2}$$

where  $V_{aS}$ ,  $V_{bS}$ , and  $V_{cS}$  show the phase voltage of phases  $a$ ,  $b$ , and  $c$ , respectively,  $R_s$  and  $L_s$  are the stator resistance and inductance, respectively, and  $e_{aS}$ ,  $e_{bS}$ , and  $e_{cS}$  indicate the corresponding phase back Electromotive Forces (EMFs) of phases  $a$ ,  $b$ , and  $c$ , respectively.

Moreover,

$$\begin{cases} V_{aG} = V_{aS} + V_{SG} \\ V_{bG} = V_{bS} + V_{SG} \\ V_{cG} = V_{cS} + V_{SG} \\ V_{SG} = 1/3(V_{aG} + V_{bG} + V_{cG}) \end{cases} \tag{3}$$

where  $V_{SG}$  represents the neutral point  $S$  to ground  $G$  voltage.

Hence, the phase voltage can be derived as follows:

$$\begin{bmatrix} V_{aS} \\ V_{bS} \\ V_{cS} \end{bmatrix} = \frac{1}{3} \begin{bmatrix} 2 & -1 & -1 \\ -1 & 2 & -1 \\ -1 & -1 & 2 \end{bmatrix} \begin{bmatrix} V_{aG} \\ V_{bG} \\ V_{cG} \end{bmatrix} \tag{4}$$

Considering Equation (4), the relationship between switching states of IGBTs and phase voltage under normal operating conditions is shown in Table 2. As a result, the following equation can be derived:

$$\begin{cases} V_{aS}^N = 1/3(SW_1(SW_4 + SW_6) - SW_2(SW_3 + SW_5))V_{DC} \\ V_{bS}^N = 1/3(SW_3(SW_2 + SW_6) - SW_4(SW_1 + SW_5))V_{DC} \\ V_{cS}^N = 1/3(SW_5(SW_2 + SW_4) - SW_6(SW_1 + SW_3))V_{DC} \end{cases} \tag{5}$$

For clarity,  $\chi^N = [\chi_1^N \ \chi_2^N \ \chi_3^N]^T$  is considered as follows:

$$\begin{cases} \chi_1^N = SW_1(SW_4 + SW_6) - SW_2(SW_3 + SW_5) \\ \chi_2^N = SW_3(SW_2 + SW_6) - SW_4(SW_1 + SW_5) \\ d\chi_3^N = SW_5(SW_2 + SW_4) - SW_6(SW_1 + SW_3) \end{cases} \tag{6}$$

Therefore, Equation (5) can be written as follows:

$$V^N = [V_{aS}^N \ V_{bS}^N \ V_{cS}^N]^T = \frac{1}{3}\chi^N V_{DC} \tag{7}$$

### B. PHASE VOLTAGE ANALYSIS UNDER FAULTY CONDITIONS

In a VSI, the switching pulses as well as the direction of the current flow determine its output voltage. Assuming that the current is positive while flowing into the PMSM winding, the switching states, the direction of current in each phase, and accordingly, the voltage of each phase of the VSI can be determined. Figure 2 shows the current paths of phase  $a$  when an open-circuit fault occurs in  $Q_1$ .

In case of an open-circuit fault in  $Q_1$ , indicated by superscript  $F_{SW_1}$ ,  $SW_1$  and  $SW_2$  are switched OFF. Taking switching state 4 into consideration, if  $i_1 > 0$ , the current of phase  $a$  flows through  $D_2$ , as shown in Figure 2(a). In this case,  $SW_1$  is switched OFF and  $SW_2$  is switched ON, which means  $V_{aG}^{F_{SW_1}} = V_{bG}^{F_{SW_1}} = V_{cG}^{F_{SW_1}} = 0$ , and accordingly,  $V_{aS}^{F_{SW_1}} = V_{bS}^{F_{SW_1}} = V_{cS}^{F_{SW_1}} = 0$ . On the contrary, if  $i_1 \leq 0$ , the current of phase  $a$  flows through  $D_1$ , as shown in Figure 2(b), which means  $SW_1$  is switched ON and  $SW_2$  is switched OFF. In this case,  $V_{aG}^{F_{SW_1}} = V_{DC}$ ,  $V_{bG}^{F_{SW_1}} = V_{cG}^{F_{SW_1}} = 0$ , and correspondingly,  $V_{aS}^{F_{SW_1}} = 2/3V_{DC}$ , and  $V_{bS}^{F_{SW_1}} = V_{cS}^{F_{SW_1}} = -1/3V_{DC}$ . Using the same procedure, the relationship between the switching states, the phase voltage, and the current direction in the case of an open-circuit fault in  $Q_1$  is derived, and the results are shown in Table 3, in which the current direction indicator  $\epsilon_x$  ( $x$  represent the corresponding phase) can be either  $\bar{\epsilon}_a$  for  $i_a > 0$  or  $\epsilon_a$  for  $i_a \leq 0$ , where  $\bar{\epsilon}_a + \epsilon_a = 1$ .

Considering the results of Table 3 and the state of  $SW_1$  and  $SW_2$ , which are both switched OFF, the phase voltage  $V_{aS}^{F_{SW_1}}$ ,  $V_{bS}^{F_{SW_1}}$ , and  $V_{cS}^{F_{SW_1}}$ , in case of an open-circuit fault in  $Q_1$  can

**TABLE 2.** The relationship between switching states and the phase voltage under normal operating conditions.

State Number	SW <sub>1</sub>	SW <sub>2</sub>	SW <sub>3</sub>	SW <sub>4</sub>	SW <sub>5</sub>	SW <sub>6</sub>	V <sub>aS</sub> <sup>N</sup>	V <sub>bS</sub> <sup>N</sup>	V <sub>cS</sub> <sup>N</sup>
0	OFF	ON	OFF	ON	OFF	ON	0	0	0
1	OFF	ON	OFF	ON	ON	OFF	-1/3V <sub>DC</sub>	-1/3V <sub>DC</sub>	2/3V <sub>DC</sub>
2	OFF	ON	ON	OFF	OFF	ON	-1/3V <sub>DC</sub>	2/3V <sub>DC</sub>	-1/3V <sub>DC</sub>
3	OFF	ON	ON	OFF	ON	OFF	-2/3V <sub>DC</sub>	1/3V <sub>DC</sub>	1/3V <sub>DC</sub>
4	ON	OFF	OFF	ON	OFF	ON	2/3V <sub>DC</sub>	-1/3V <sub>DC</sub>	-1/3V <sub>DC</sub>
5	ON	OFF	OFF	ON	ON	OFF	1/3V <sub>DC</sub>	-2/3V <sub>DC</sub>	1/3V <sub>DC</sub>
6	ON	OFF	ON	OFF	OFF	ON	1/3V <sub>DC</sub>	1/3V <sub>DC</sub>	-2/3V <sub>DC</sub>
7	ON	OFF	ON	OFF	ON	OFF	0	0	0

**TABLE 3.** The relationship between switching states, phase voltage, and current direction in case of an open-circuit fault in Q<sub>1</sub>.

State Number	SW <sub>1</sub>	SW <sub>2</sub>	SW <sub>3</sub>	SW <sub>4</sub>	SW <sub>5</sub>	SW <sub>6</sub>	ε <sub>a</sub>	V <sub>aS</sub> <sup>F<sub>sw1</sub></sup>	V <sub>bS</sub> <sup>F<sub>sw1</sub></sup>	V <sub>cS</sub> <sup>F<sub>sw1</sub></sup>
4	OFF	OFF	OFF	ON	OFF	ON	$\bar{\epsilon}_a$	0	0	0
							$\underline{\epsilon}_a$	2/3V <sub>DC</sub>	-1/3V <sub>DC</sub>	-1/3V <sub>DC</sub>
5	OFF	OFF	OFF	ON	ON	OFF	$\bar{\epsilon}_a$	-1/3V <sub>DC</sub>	-1/3V <sub>DC</sub>	2/3V <sub>DC</sub>
							$\underline{\epsilon}_a$	1/3V <sub>DC</sub>	-2/3V <sub>DC</sub>	1/3V <sub>DC</sub>
6	OFF	OFF	ON	OFF	OFF	ON	$\bar{\epsilon}_a$	-1/3V <sub>DC</sub>	2/3V <sub>DC</sub>	-1/3V <sub>DC</sub>
							$\underline{\epsilon}_a$	1/3V <sub>DC</sub>	1/3V <sub>DC</sub>	-2/3V <sub>DC</sub>
7	OFF	OFF	ON	OFF	ON	OFF	$\bar{\epsilon}_a$	-2/3V <sub>DC</sub>	1/3V <sub>DC</sub>	1/3V <sub>DC</sub>
							$\underline{\epsilon}_a$	0	0	0

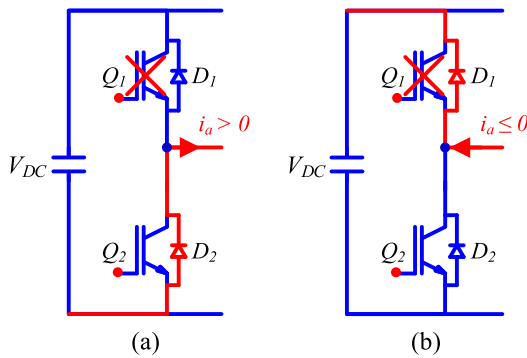


**FIGURE 2.** The current paths of phase *a* in case of an open-circuit fault in Q<sub>1</sub>: (a) *i<sub>a</sub>* > 0, and (b) *i<sub>a</sub>* ≤ 0.

be formulated as follows:

$$\begin{cases} V_{aS}^{F_{sw1}} = 1/3 \left( (SW_4 + SW_6)\underline{\epsilon}_a - (SW_3 + SW_5)\bar{\epsilon}_a \right) V_{DC} \\ V_{bS}^{F_{sw1}} = 1/3 \left( SW_3(SW_6 + \bar{\epsilon}_a) - SW_4(SW_5 + \underline{\epsilon}_a) \right) V_{DC} \\ V_{cS}^{F_{sw1}} = 1/3 \left( SW_5(SW_4 + \bar{\epsilon}_a) - SW_6(SW_3 + \underline{\epsilon}_a) \right) V_{DC} \end{cases} \quad (8)$$

An open-circuit fault in Q<sub>2</sub> directly affects switching states 0, 1, 2, and 3. Likewise, the relationship between the switching states, the phase voltage, and current direction in the case of an open-circuit fault in Q<sub>2</sub> can be derived, which is exactly the same as the results of the open-circuit fault in Q<sub>1</sub>. Thus, the phase voltage equation in case of an open-circuit

fault in phase *a*, i.e., either an open-circuit fault in SW<sub>1</sub> or SW<sub>2</sub>, is derived as follows:

$$\begin{cases} V_{aS}^{F_a} = 1/3 \left( (SW_4 + SW_6)\underline{\epsilon}_a - (SW_3 + SW_5)\bar{\epsilon}_a \right) V_{DC} \\ V_{bS}^{F_a} = 1/3 \left( SW_3(SW_6 + \bar{\epsilon}_a) - SW_4(SW_5 + \underline{\epsilon}_a) \right) V_{DC} \\ V_{cS}^{F_a} = 1/3 \left( SW_5(SW_4 + \bar{\epsilon}_a) - SW_6(SW_3 + \underline{\epsilon}_a) \right) V_{DC} \end{cases} \quad (9)$$

Considering  $\chi^{F_a} = [\chi_1^{F_a} \ \chi_2^{F_a} \ \chi_3^{F_a}]^T$  as Equation (10), Equation (11) is obtained.

$$\begin{cases} \chi_1^{F_a} = (SW_4 + SW_6)\underline{\epsilon}_a - (SW_3 + SW_5)\bar{\epsilon}_a \\ \chi_2^{F_a} = SW_3(SW_6 + \bar{\epsilon}_a) - SW_4(SW_5 + \underline{\epsilon}_a) \\ \chi_3^{F_a} = SW_5(SW_4 + \bar{\epsilon}_a) - SW_6(SW_3 + \underline{\epsilon}_a) \end{cases} \quad (10)$$

$$V^{F_a} = [V_{aS}^{F_a} \ V_{bS}^{F_a} \ V_{cS}^{F_a}]^T = \frac{1}{3} \chi^{F_a} V_{DC} \quad (11)$$

Using the same procedure and considering  $\bar{\epsilon}_b$  for *i<sub>b</sub>* > 0 and  $\underline{\epsilon}_b$  for *i<sub>b</sub>* ≤ 0, where  $\bar{\epsilon}_b + \underline{\epsilon}_b = 1$ , and  $\bar{\epsilon}_c$  for *i<sub>c</sub>* > 0 and  $\underline{\epsilon}_c$  for *i<sub>c</sub>* ≤ 0, where  $\bar{\epsilon}_c + \underline{\epsilon}_c = 1$ , the phase voltage equations in case of open-circuit faults in phases *b* and *c*, i.e., *V<sup>F<sub>b</sub></sup>* and *V<sup>F<sub>c</sub></sup>*, are respectively obtained as follows:

$$\begin{cases} V_{aS}^{F_b} = 1/3 \left( SW_1(SW_6 + \bar{\epsilon}_b) - SW_2(SW_5 + \underline{\epsilon}_b) \right) V_{DC} \\ V_{bS}^{F_b} = 1/3 \left( (SW_2 + SW_6)\underline{\epsilon}_b - (SW_1 + SW_5)\bar{\epsilon}_b \right) V_{DC} \\ V_{cS}^{F_b} = 1/3 \left( SW_5(SW_2 + \bar{\epsilon}_b) - SW_6(SW_1 + \underline{\epsilon}_b) \right) V_{DC} \end{cases} \quad (12)$$

$$\begin{cases} V_{aS}^{Fc} = 1/3(SW_1(SW_4 + \overline{\epsilon_c}) - SW_2(SW_3 + \underline{\epsilon_c}))V_{DC} \\ V_{bS}^{Fc} = 1/3(SW_3(SW_2 + \overline{\epsilon_c}) - SW_4(SW_1 + \underline{\epsilon_c}))V_{DC} \\ V_{cS}^{Fc} = 1/3((SW_2 + SW_4)\underline{\epsilon_c} - (SW_1 + SW_3)\overline{\epsilon_c})V_{DC} \end{cases} \quad (13)$$

It should be noted that in case of open-circuit faults in phases *b* and *c*, paired switches (*SW*<sub>3</sub> and *SW*<sub>4</sub>) and (*SW*<sub>5</sub> and *SW*<sub>6</sub>) are respectively switched OFF. Therefore, they are omitted from Equations (12) and (13).

Considering  $\chi^{Fb} = [\chi_1^{Fb} \ \chi_2^{Fb} \ \chi_3^{Fb}]^T$  as Equation (14) and  $\chi^{Fc} = [\chi_1^{Fc} \ \chi_2^{Fc} \ \chi_3^{Fc}]^T$  as Equation (15), Equations (16) and (17) are derived.

$$\begin{cases} \chi_1^{Fb} = SW_1(SW_6 + \overline{\epsilon_b}) - SW_2(SW_5 + \underline{\epsilon_b}) \\ \chi_2^{Fb} = (SW_2 + SW_6)\underline{\epsilon_b} - (SW_1 + SW_5)\overline{\epsilon_b} \\ \chi_3^{Fb} = SW_5(SW_2 + \overline{\epsilon_b}) - SW_6(SW_1 + \underline{\epsilon_b}) \end{cases} \quad (14)$$

$$\begin{cases} \chi_1^{Fc} = SW_1(SW_4 + \overline{\epsilon_c}) - SW_2(SW_3 + \underline{\epsilon_c}) \\ \chi_2^{Fc} = SW_3(SW_2 + \overline{\epsilon_c}) - SW_4(SW_1 + \underline{\epsilon_c}) \\ \chi_3^{Fc} = (SW_2 + SW_4)\underline{\epsilon_c} - (SW_1 + SW_3)\overline{\epsilon_c} \end{cases} \quad (15)$$

$$V^{Fb} = [V_{aS}^{Fb} \ V_{bS}^{Fb} \ V_{cS}^{Fb}]^T = \frac{1}{3}\chi^{Fb}V_{DC} \quad (16)$$

$$V^{Fc} = [V_{aS}^{Fc} \ V_{bS}^{Fc} \ V_{cS}^{Fc}]^T = \frac{1}{3}\chi^{Fc}V_{DC} \quad (17)$$

### C. ELECTRIC DRIVE-MOTOR SYSTEMS MODELING AND CONTROL

In order to create a stator flux vector in a PMSM, the three-phase sinusoidal current, i.e., *i<sub>a</sub>*, *i<sub>b</sub>*, and *i<sub>c</sub>*, should be controlled. Independent control of three-phase sinusoidal current requires complex mathematical calculations to trace and regulate the sinusoidal reference signal. FOC is an efficient method to simplify such mathematical calculations by transforming the three-phase stationary system (*abc*) to a rotating synchronous with the rotor system (*dq*). In fact, FOC decomposes the three-phase stator current into two main components, i.e., magnetic field generation (*d*-axis) and torque generation (*q*-axis), which can be controlled separately.

According to Figure (1) and assuming sinusoidal three-phase distributed winding and by neglecting the effect of magnetic saturation and leaking inductances, the stator voltage equation can be written as follows:

$$\begin{bmatrix} V_a \\ V_b \\ V_c \end{bmatrix} = R_s \begin{bmatrix} i_a \\ i_b \\ i_c \end{bmatrix} + \frac{d}{dt} \begin{bmatrix} \psi_a \\ \psi_b \\ \psi_c \end{bmatrix} \quad (18)$$

where *V<sub>a</sub>*, *V<sub>b</sub>*, and *V<sub>c</sub>* are the phase voltage across each stator winding, and  $\psi_a$ ,  $\psi_b$ , and  $\psi_c$  are the magnetic flux in each stator winding.

In addition,

$$\begin{bmatrix} \psi_a \\ \psi_b \\ \psi_c \end{bmatrix} = \begin{bmatrix} L_{aa} & L_{ab} & L_{ac} \\ L_{ba} & L_{bb} & L_{bc} \\ L_{ca} & L_{cb} & L_{cc} \end{bmatrix} \begin{bmatrix} i_a \\ i_b \\ i_c \end{bmatrix} + \psi_m \begin{bmatrix} \cos\theta_e \\ \cos(\theta_e - \frac{2\pi}{3}) \\ \cos(\theta_e + \frac{2\pi}{3}) \end{bmatrix} \quad (19)$$

where *L<sub>aa</sub>*, *L<sub>bb</sub>*, and *L<sub>cc</sub>* represent the self-inductances of each stator winding, *L<sub>ab</sub>*, *L<sub>ac</sub>*, *L<sub>ba</sub>*, *L<sub>bc</sub>*, *L<sub>ca</sub>*, and *L<sub>cb</sub>* are the mutual inductances of the stator windings, and  $\psi_m$  indicates the permanent magnet flux linkage.

Applying Park's transformation, the stator winding voltage and current equations in the *dq*-reference frame can be written as follows:

$$\begin{bmatrix} V_d \\ V_q \\ V_0 \end{bmatrix} = \frac{2}{3} \begin{bmatrix} \cos\theta_e & \cos(\theta_e - \frac{2\pi}{3}) & \cos(\theta_e + \frac{2\pi}{3}) \\ -\sin\theta_e & -\sin(\theta_e - \frac{2\pi}{3}) & -\sin(\theta_e + \frac{2\pi}{3}) \\ 1/2 & 1/2 & 1/2 \end{bmatrix} \times \begin{bmatrix} V_a \\ V_b \\ V_c \end{bmatrix} \quad (20)$$

$$\begin{bmatrix} i_d \\ i_q \\ i_0 \end{bmatrix} = \frac{2}{3} \begin{bmatrix} \cos\theta_e & \cos(\theta_e - \frac{2\pi}{3}) & \cos(\theta_e + \frac{2\pi}{3}) \\ -\sin\theta_e & -\sin(\theta_e - \frac{2\pi}{3}) & -\sin(\theta_e + \frac{2\pi}{3}) \\ 1/2 & 1/2 & 1/2 \end{bmatrix} \times \begin{bmatrix} i_a \\ i_b \\ i_c \end{bmatrix} \quad (21)$$

Defining  $L_d = L_s + M_s + \frac{2}{3}L_m$ ,  $L_q = L_s + M_s - \frac{2}{3}L_m$ , and  $L_0 = L_s - 2M_s$ , Equation (20) can be rewritten as follows:

$$\begin{cases} V_d = R_s i_d + L_d \frac{di_d}{dt} - N\omega i_q L_q \\ V_q = R_s i_q + L_q \frac{di_q}{dt} + N\omega (i_d L_d + \psi_m) \\ V_0 = R_s i_0 + L_0 \frac{di_0}{dt} \end{cases} \quad (22)$$

where *L<sub>d</sub>* and *L<sub>q</sub>* are the stator *d*-axis and *q*-axis inductances, respectively, *L<sub>0</sub>* is the stator zero-sequence inductance, *N* shows the number of rotor permanent magnet pole pairs, *M<sub>s</sub>* is the stator mutual inductance, and *L<sub>m</sub>* shows the stator inductance fluctuation.

Correspondingly, the rotor torque *T<sub>e</sub>* is derived as follows:

$$T_e = \frac{3}{2}N (i_q(i_d L_d + \psi_m) - i_d i_q L_q) \quad (23)$$

In addition,

$$\frac{d\omega}{dt} = \frac{N}{J} (T_e - B\omega - T_m) \quad (24)$$

where *J* shows the rotor moment of inertia, *B* is the viscous friction factor, and *T<sub>m</sub>* is the mechanical torque.

The stator flux vector is perpendicular to the rotor flux vector. Hence, the desired value of *i<sub>d</sub>* is zero, and accordingly, the stator reference current in the *d*-axis, i.e., *i<sub>d</sub><sup>\*</sup>*, is equal to zero. Therefore, Equation (24) can be rewritten as follows:

$$T_e = \frac{3}{2}N i_q \psi_m \quad (25)$$

Considering Equations (24) and (25), the stator reference current in *q*-axis *i<sub>q</sub><sup>\*</sup>* can be derived as follows:

$$i_q^* = \frac{2}{3N\psi_m} (B\omega + T_m + \frac{J}{N} \frac{d\omega}{dt}) \quad (26)$$

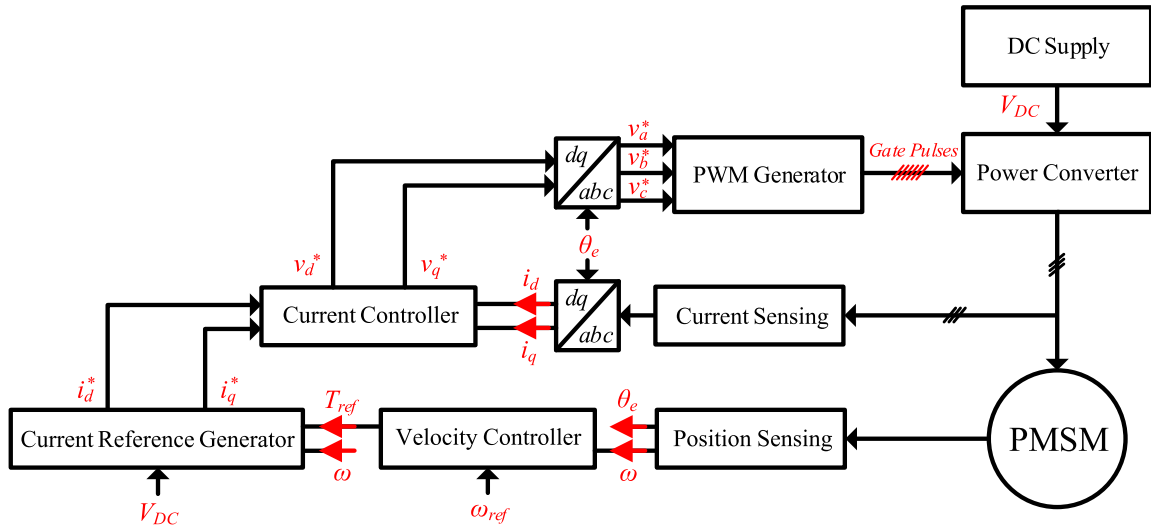


FIGURE 3. The diagram of the sensed FOC of three-phase PMSM.

Accordingly, the feedforward stator voltage equations can be written as follows:

$$\begin{cases} v_d^* = R_s i_d - L_q \omega i_q + L_d \frac{di_d}{dt} + \frac{d\psi_m}{dt} \\ v_q^* = R_s i_q + L_d \omega i_d + L_q \frac{di_q}{dt} + \psi_m \omega \end{cases} \quad (27)$$

Figure (3) shows the diagram of the sensed FOC of three-phase PMSM. Based on the presented closed-loop control, the reference angular velocity  $\omega_{ref}$  is compared with the measured angular velocity to determine the angular velocity error signal. Using a Proportional-Integral (PI) controller, the angular velocity error is processed and the output is the reference torque ( $T_{ref}$ ) to achieve the desired velocity control performance. The current reference generator is a function of rotor angular velocity, the reference torque, and the DC-link voltage of the power converter, and it can generate the stator reference current in the  $dq$ -axis. Once the stator reference current signals are obtained, the current controller generates the reference voltage signals in the  $dq$ -axis ( $v_d^*$  and  $v_q^*$ ), which are indeed compensated by feedforward terms to enhance the system response. The generated reference voltage signals are transformed into the  $abc$  domain as the inputs of the Pulse Width Modulation (PWM) generator to generate the gate pulses.

The voltage equation for each phase of the PMSM can be written as follows:

$$\begin{bmatrix} V_{aS} \\ V_{bS} \\ V_{cS} \end{bmatrix} = R_s \begin{bmatrix} i_a \\ i_b \\ i_c \end{bmatrix} + L_s \frac{d}{dt} \begin{bmatrix} \frac{di_a}{dt} \\ \frac{di_b}{dt} \\ \frac{di_c}{dt} \end{bmatrix} + \begin{bmatrix} e_{aS} \\ e_{bS} \\ e_{cS} \end{bmatrix} \quad (28)$$

where

$$\begin{bmatrix} e_{aS} \\ e_{bS} \\ e_{cS} \end{bmatrix} = -\omega \psi_m \begin{bmatrix} \sin \theta_e \\ \sin(\theta_e - \frac{2}{3}\pi) \\ \sin(\theta_e + \frac{2}{3}\pi) \end{bmatrix} \quad (29)$$

Taking Equations (7), (11), (16), (17) into account, the phase voltage function can be written as follows:

$$V = [V_{aS} \ V_{bS} \ V_{cS}]^T = \frac{1}{3} \chi V_{DC} \quad (30)$$

where  $\chi = f(\chi^N \ \chi^{F_a} \ \chi^{F_b} \ \chi^{F_c})$ .

Considering the phase current as the state variables, the corresponding state-space description of the system is derived as Equation (31), as shown at the bottom of the next page, where  $A$ ,  $B$ , and  $H$  are the system matrices.

### III. PROPOSED OPEN-CIRCUIT FAULT DIAGNOSIS APPROACH

The proposed open-circuit fault diagnosis approach consists of three main stages, namely fault detection, fault localization, and fault clearance.

#### A. FAULT DETECTION STAGE

According to Equation (1), under normal operating conditions, the summation of the stator current should be equal to zero. Since the current measurements may not be accurate, a threshold  $\varepsilon_0$  is defined to ensure the correct measurement of the state variables by the current sensors, as follows:

$$|i_a + i_b + i_c| < \varepsilon_0 \quad (32)$$

It is indeed not guaranteed that Equation (32) can clearly determine the proper operation of all current sensors. Therefore, an effective fault detection procedure requires additional information in arriving at a decision and detecting abnormalities or faults.

An open-circuit fault in the VSI-fed PMSM drive system significantly changes the last term in Equation (31), i.e.,  $H\chi$ , and leads to a considerable deviation between the actual measured and estimated state variables. Using an observer constructed based on the system's model under normal operating conditions, open-circuit faults are detected

by monitoring the residuals and declaring a fault when they cross a certain threshold.

Under normal operating conditions,  $\chi^N = \chi$ . Considering Equation (31), the current residual function can be written as follows:

$$\frac{d}{dt}(i_x - i_x^N) = A(i_x - i_x^N) + H(\chi_x - \chi^N) \quad (33)$$

where superscript  $N$  and subscript  $x$  show the parameters under normal operating conditions and phase number, respectively.

An open-circuit fault is detected when  $|i_x - i_x^N| \geq \varepsilon_d$ , where  $\varepsilon_d$  represents the open-circuit fault detection threshold.

**B. FAULT LOCALIZATION STAGE**

After detecting an open-circuit fault, an online data-driven approach, called the MMC-SVM algorithm with RBF kernel function, is used to locate such a fault. The collected data by the current sensors is affected by many factors, such as temperature, and indeed, the collected dataset contains noisy data [48]. The determining factor in the development of the proposed data-driven algorithm to successfully localize open-circuit faults is to properly collect the data.

The collected dataset contains the real-time three-phase current signal of the VSI-fed PMSM drive system. Each column in the collected dataset represents a certain feature. The redundant data in the collected dataset is removed to improve the accuracy of the fault diagnosis process and minimize the computation time. The feature set is normalized to generate the training dataset, i.e., support vectors, and test dataset. Since the collected dataset is not linearly separable, the RBF kernel function is used for training the MMC-SVM model, as follows [49], [50], [51]:

$$K(i_x, i_x^N) = e^{-\lambda |i_x - i_x^N|^2} \quad (34)$$

where  $K$  represents the kernel function, and  $\lambda$  is a positive value.

The term  $|i_x - i_x^N|^2$  shows the squared Euclidean distance between the actual measured phase current and the phase current under normal operating conditions. In particular, under normal operating conditions,  $i_x \approx i_x^N$ , and thus, the difference between two vectors becomes zero. As a result, the exponential term in Equation (34) becomes approximately equal to 1. On the contrary, if  $i_x \not\approx i_x^N$ , the difference between two vectors becomes a large number, and according to Equation (34), the exponential term becomes roughly equal to zero. In addition, if a large positive value is considered for  $\lambda$ ,

the proposed method may misclassify the training dataset and increase the risk of overfitting. Hence, the proposed MMC-SVM decision boundary depends on the points close to a predefined hyperplane, and indeed, the points that are far away from the decision boundary are ignored. As a matter of fact,  $\lambda$  determines how far the influence of a single training data reaches and it is a function of the standard deviation of the collected dataset, as follows:

$$\lambda = \frac{1}{2\sigma^2} \quad (35)$$

where  $\sigma$  is a free parameter and depends on the variance of the collected data [49].

To deal with large numbers of training samples/features, the Taylor series expansion of the kernel function is employed. For clarity, if  $\sigma = 1$  in Equation (34), Equation (36), as shown at the bottom of the next page, can be derived. Using the Taylor series expansion, the second term in Equation (36) can be written as Equation (37), as shown at the bottom of the next page, in which  $n$  represents the length of the data sequence. Using the dot product, Equation (37) can be rewritten as Equation (38), as shown at the bottom of the next page. Therefore, Equation (34) can be rewritten as Equation (39), as shown at the bottom of the next page. By defining  $M$ , as shown in Equation (39), Equation (40), as shown at the bottom of the next page, can be derived, which shows the relationship between the two corresponding values of the points in two vectors in infinite dimensions. Similarly, the MMC-SVM model can be trained using any  $\lambda$ , and by testing under different conditions, the corresponding labels for evaluation can be predicted.

Unlike autoencoders, the proposed MMC-SVM model is a supervised learning-based approach, and a label is assigned to each data point in the dataset. Particularly, when an open-circuit fault is detected, initially, the fault data from different fault locations are generated, and after training the MMC-SVM model using Equation (34), a hyperplane is determined to separate the classes and maximize the squared Euclidean distance between the closet data points related to each class and the decision boundary. As a result, the corresponding labels for all data points in the dataset are predicted, and the accurate location of the open-circuit fault is determined.

**C. FAULT CLEARANCE STAGE**

Figure 4 shows the proposed open-circuit fault clearance strategy for the VSI-fed PMSM drive system, in which  $S_1, \dots, S_6$  are the backup switches in series connection with backup IGBTs. Under normal operating conditions,

$$\begin{bmatrix} \frac{di_a}{dt} \\ \frac{di_b}{dt} \\ \frac{di_c}{dt} \end{bmatrix} = \underbrace{\begin{bmatrix} -R_s/L_s & 0 & 0 \\ 0 & -R_s/L_s & 0 \\ 0 & 0 & -R_s/L_s \end{bmatrix}}_A \begin{bmatrix} i_a \\ i_b \\ i_c \end{bmatrix} + \underbrace{\begin{bmatrix} -1/L_s & 0 & 0 \\ 0 & -1/L_s & 0 \\ 0 & 0 & -1/L_s \end{bmatrix}}_B \begin{bmatrix} e_{aS} \\ e_{bS} \\ e_{cS} \end{bmatrix} + \underbrace{\begin{bmatrix} v_{bc}/3L_s \\ v_{bc}/3L_s \\ v_{bc}/3L_s \end{bmatrix}}_H \chi \quad (31)$$

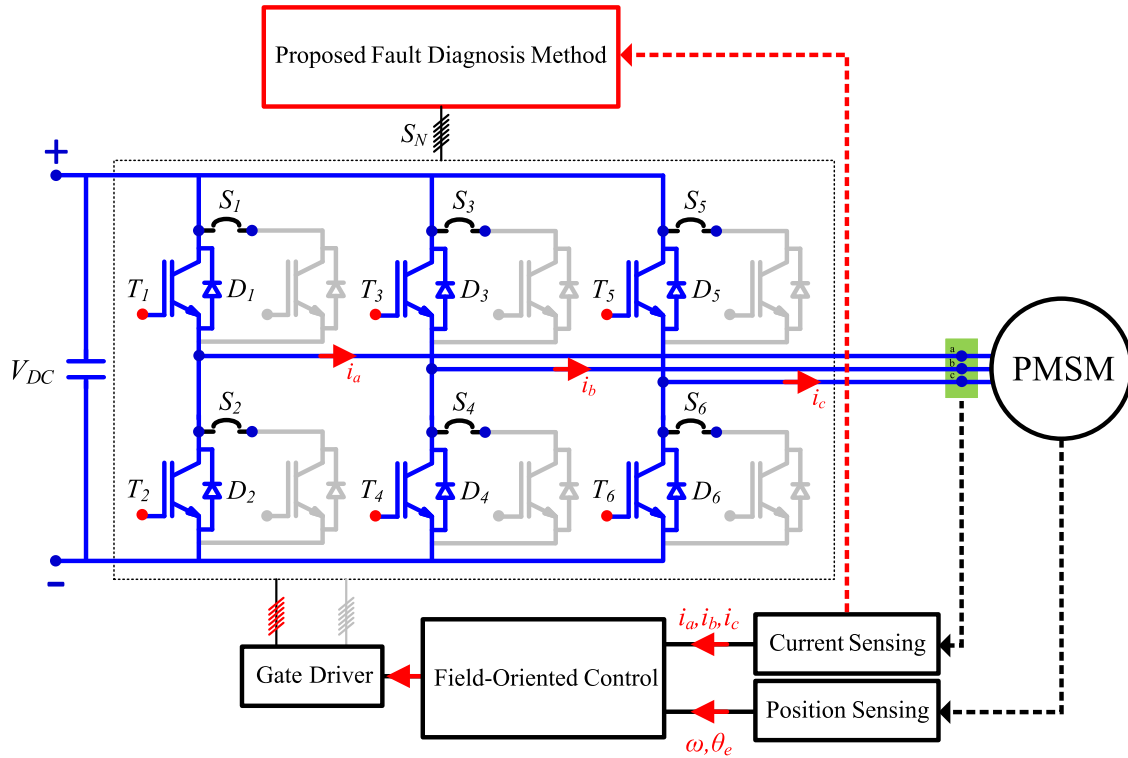


FIGURE 4. The proposed open-circuit fault clearance strategy for the VSI-fed PMSM drive system.

the backup switches are normally opened and the backup IGBTs are idle while receiving the gate pulses. Once the open-circuit fault is detected and located, the faulty IGBT is bypassed by closing the corresponding backup switch, and then, the current flows through the parallel path with the faulty IGBT. Since no reconfiguration is needed, the gate pulses are automatically modified to ensure a stable and continuous operation of the VSI-fed PMSM drive system without major waveform distortions and/or overcurrent issues. It should be noted that the restoration to normal operating conditions highly depends on the open-circuit fault duration and if such a fault persistently exists, fault clearance and restoration to normal operating conditions may not be possible.

IV. RESULTS AND DISCUSSION

In order to check the performance of the proposed open-circuit fault diagnosis method, a PMSM propelling an HEV in series architecture is investigated. The studied series HEV consists of an ICE, battery pack, VSI, and PMSM, in which the ICE drives the electric generator instead of driving the wheels. Correspondingly, an electric generator charges the battery pack and supplies power to the PMSM to move the HEV. If a large amount of power is required, the PMSM absorbs electricity from both the battery pack and the electric generator. A DC/DC converter is connected to the battery pack and feeds the PMSM through a three-phase VSI. As the ICE only generates electricity for the electric motor, series HEVs are referred to as Extended-Range Electric

$$K(i_x, i_x^N) = e^{-\frac{(i_x - i_x^N)^2}{2}} = e^{-\frac{(i_x)^2 + (i_x^N)^2 - 2i_x i_x^N}{2}} = e^{-\frac{1}{2}(i_x)^2 + i_x i_x^N} \tag{36}$$

$$e^{i_x i_x^N} = 1 + \frac{1}{1!}(i_x i_x^N) + \frac{1}{2!}(i_x i_x^N)^2 + \frac{1}{3!}(i_x i_x^N)^3 + \dots + \frac{1}{n!}(i_x i_x^N)^n \tag{37}$$

$$e^{i_x i_x^N} = \left(1, \sqrt{\frac{1}{1!}}i_x, \sqrt{\frac{1}{2!}}(i_x)^2, \dots, \sqrt{\frac{1}{n!}}(i_x)^n\right) \cdot \left(1, \sqrt{\frac{1}{1!}}i_x^N, \sqrt{\frac{1}{2!}}(i_x^N)^2, \dots, \sqrt{\frac{1}{n!}}(i_x^N)^n\right) \tag{38}$$

$$e^{-\frac{(i_x - i_x^N)^2}{2}} = \underbrace{e^{-\frac{1}{2}(i_x)^2 + (i_x)^2 i_x^N}}_M \left[ \left(1, \sqrt{\frac{1}{1!}}i_x, \sqrt{\frac{1}{2!}}(i_x)^2, \dots, \sqrt{\frac{1}{n!}}(i_x)^n\right) \cdot \left(1, \sqrt{\frac{1}{1!}}i_x^N, \sqrt{\frac{1}{2!}}(i_x^N)^2, \dots, \sqrt{\frac{1}{n!}}(i_x^N)^n\right) \right] \tag{39}$$

$$e^{-\frac{(i_x - i_x^N)^2}{2}} = \left(M, M\sqrt{\frac{1}{1!}}i_x, M\sqrt{\frac{1}{2!}}(i_x)^2, \dots, M\sqrt{\frac{1}{n!}}(i_x)^n\right) \cdot \left(M, M\sqrt{\frac{1}{1!}}i_x^N, M\sqrt{\frac{1}{2!}}(i_x^N)^2, \dots, M\sqrt{\frac{1}{n!}}(i_x^N)^n\right) \tag{40}$$

TABLE 4. ICE parameters.

Parameters	Values
Maximum Power ( $P_m^{\max}$ )	115 kW
Maximum Torque ( $T_m^{\max}$ )	280 N·m
Gain for ICE Model	178.3
Time Constant for ICE Model	0.1 s

TABLE 5. Vehicle parameters.

Parameters	Values
Vehicle Mass ( $M_v$ )	1100 kg
Gravitational Acceleration ( $g$ )	9.8 m/s <sup>2</sup>
Air Density ( $\rho_a$ )	1.2 kg/m <sup>3</sup>
Maximum Vehicle Cross-Section Area	0.9 m <sup>2</sup>
Air Drag	0.4 N·s <sup>2</sup> /kg·m
Rolling Coefficients ( $cr_1$ and $cr_2$ )	0.1 and 0.2
Gear Reduction Ratio	9
Wheel Radius ( $r_w$ )	0.3 m

TABLE 6. Electric drive parameters.

Parameters	Values
Maximum Power ( $P_e^{\max}$ )	35 kW
Maximum Torque ( $T_e^{\max}$ )	205 N·m
Stator $d$ -Axis Inductance ( $L_d$ )	0.00024368 H
Stator $q$ -Axis Inductance ( $L_q$ )	0.00029758 H
Stator Zero-Sequence Inductance ( $L_0$ )	0.00012184 H
Stator Resistance Per Phase ( $R_s$ )	0.010087 $\Omega$
Permanent Magnet Flux Linkage ( $\psi_m$ )	0.04366 Wb
Number of Pole Pairs ( $N$ )	8
Rotor Moment of Inertia ( $J$ )	0.1234 kg·m <sup>2</sup>
DC-Link Capacitor ( $C_{DC}$ )	0.001 F
Nominal Voltage ( $V_N$ )	352 V
Switching Frequency ( $f_{sw}$ )	10 kHz

TABLE 7. Battery pack parameters.

Parameters	Values
Battery Pack Capacity ( $Q_B$ )	30000 W·h
Battery Pack Nominal Voltage ( $V_B$ )	260 V
Internal Resistance ( $R_i$ )	0.001 $\Omega$
Initial Charge	80.75 A·h
Initial State-of-Charge	70%
Battery Rating	115 A·h

Vehicles (EREVs). A fixed-ratio gear-reduction model is used to implement the vehicle transmission and differential systems. The driving inputs, including steering and braking, and other conditions, such as wind speed and road slope, are converted into different commands for the generator and PMSM using a vehicle control system. Overall, the main objective is to control the torque of the PMSM. Tables 4 to 7

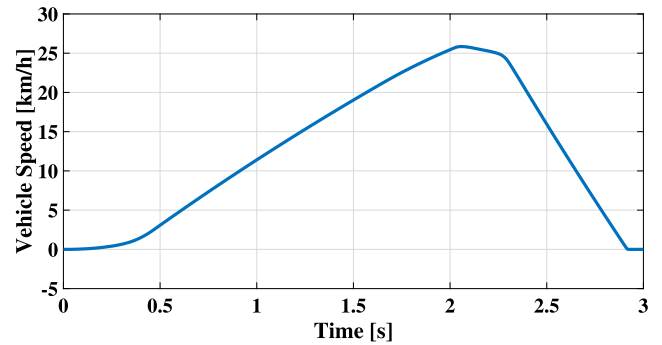


FIGURE 5. The vehicle speed under normal operating conditions.

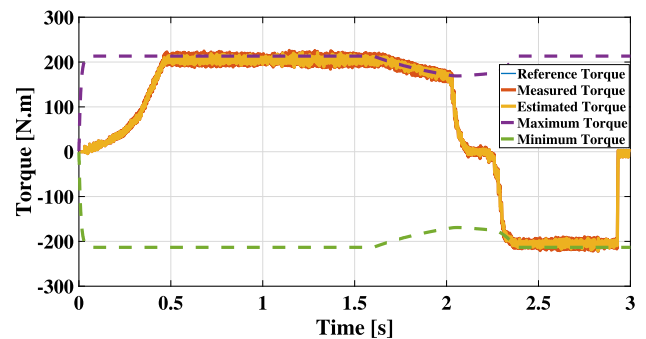


FIGURE 6. The PMSM reference, measured, estimated, maximum and minimum torques under normal operating conditions.

show the parameters of the studied ICE, vehicle, electric drive, and battery pack, respectively.

### A. NORMAL OPERATING CONDITIONS

It is assumed that the HEV is accelerating on a straight road between 0.45 and 2.0 s, and during this time period, its velocity increases from 0 to 25.8 km/h. For 0.20 s, the velocity gradually decreases, and at 2.20 s, the brake is applied, which leads to a reduction in the velocity of the HEV to 0 km/h. Figures 5 to 7 show the vehicle speed, PMSM torque, and three-phase current under normal operating conditions, respectively. It is also noted that under normal operating conditions, the DC-link voltage is regulated at 338.14 V and the State-of-Charge (SoC) of the battery pack is slightly increased from 70% to 70.052%. Figure 8 illustrates the residual current under normal operating conditions. Performing a series of experiments,  $\varepsilon_d = 20$  and  $\varepsilon_l = e^{-10}$  are selected as the open-circuit fault detection and location thresholds, respectively. Such values are selected in such a way as to improve the accuracy of the diagnosis process, reduce overfitting, prevent the wrong diagnosis, and minimize the computational burden.

As shown in Figure 9, since no open-circuit fault is detected, the diagnostic variables, called fault detection flag, which can be either 0 or 1, and fault localization flag, which shows one of the six switches (or multiple switches), are both zero. The fault detection flag is zero because the current residuals are less than the predefined open-circuit fault detection threshold. In addition, according to the exponential

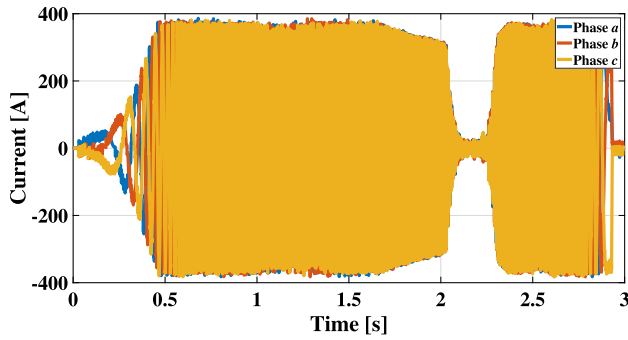


FIGURE 7. The three-phase current of the PMSM under normal operating conditions.

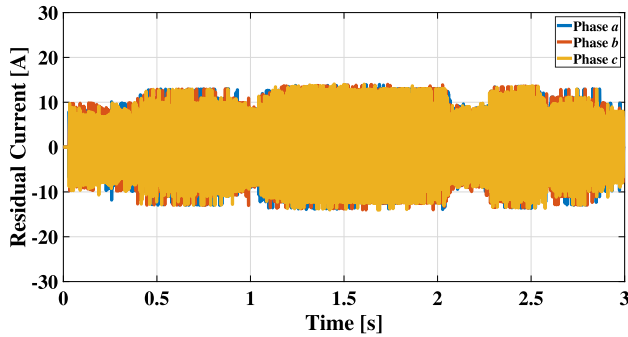


FIGURE 8. The three-phase residual current of the PMSM under normal operating conditions.

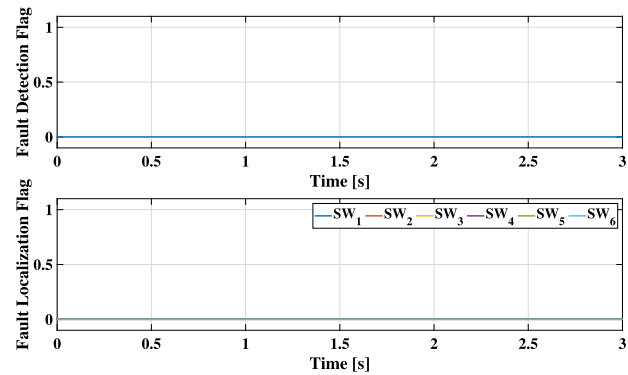


FIGURE 9. The diagnostic variables under normal operating conditions.

term in Equation 34 and defining  $\lambda = 0.0576$ , the difference between the measured and estimated current signals becomes very small, and accordingly, the fault localization flag for all switches is null.

### B. OPEN-CIRCUIT FAULT IN SINGLE SWITCH

It is assumed that at  $t = 1$  s, an open-circuit fault occurs in the first switch ( $SW_1$ ) and persistently exits till the end of simulation time. Figure 10 shows the three-phase current of the PMSM in case of an open-circuit fault in  $SW_1$ , in which no current limiter is used to clearly indicate the Rate of Rise (RoR) of the three-phase current. The open-circuit fault in  $SW_1$  causes an increase in the current of phases  $b$  and  $c$  by 78% and 70%, respectively.

Changes in the vehicle speed directly cause a significant increase in the current of phases  $b$  and  $c$  by roughly 8 times,

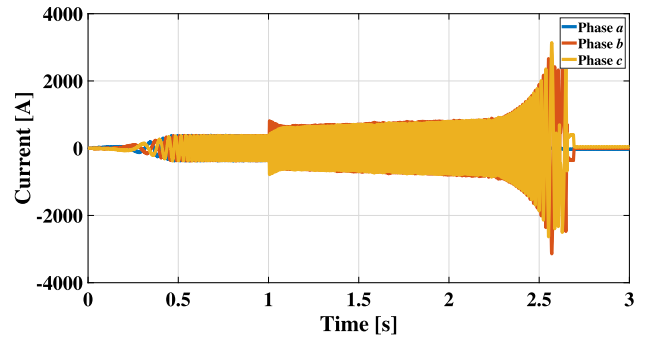


FIGURE 10. The three-phase current of the PMSM in case of an open-circuit fault in  $SW_1$ .

and indeed, if no protection measures are practically taken, such a destructive increase in the phases current can cause severe physical damage to the PMSM windings, as well as to the VSI. As a result of such a fault, as shown in Figure 11, the PMSM measured and estimated torques significantly change, and also, the current residuals exceed the predefined open-circuit fault detection threshold, and correspondingly, the fault detection flag changes to 1 within 0.01 ms to indicate the fault occurrence. Figure 12 demonstrates the three-phase residual current of the PMSM in case of an open-circuit fault in  $SW_1$ . Since the MMC-SVM algorithm is trained with a set of faulty scenarios, using Equation 34, the exponential terms related to  $SW_2$  to  $SW_6$  exceed the fault localization threshold, and correspondingly, the fault localization flag shows an open-circuit fault in  $SW_1$ . Figure 13 illustrates the diagnostic variables in case of an open-circuit fault in  $SW_1$ . The open-circuit fault in  $SW_1$  is detected and located within 0.5 ms, which is approximately  $1/16$  of the phase current fundamental wave period.

Once the open-circuit fault in  $SW_1$  is detected and located, according to Figure 4, the corresponding backup switch, i.e.,  $S_1$ , which is in series connection with a backup IGBT, bypasses the fault, and as shown in Figure 14, clears the fault. As mentioned earlier, there is a strict time period to clear the fault, i.e., 2 ms, and if the fault is not cleared within the mentioned time period, the VSI-fed PMSM drive system becomes uncontrollable. As an open-circuit fault in  $SW_1$  is detected, the fault detection and localization flags maintain their previous conditions, but the VSI-fed PMSM drive system restores to its normal operating conditions. In addition, Figure 14 illustrates that the open-circuit fault in  $SW_1$  is cleared within 0.5 ms. Figure 15 shows the residual current after clearing the open-circuit fault in  $SW_1$ . As a result of such an open-circuit fault, the current residuals exceed the predefined threshold, but the VSI-fed PMSM drive system continues its normal operating conditions.

### C. BACK-TO-BACK OPEN-CIRCUIT FAULTS IN MULTIPLE SWITCHES

In the second scenario, it is assumed that open-circuit faults in two switches  $SW_5$  (an upper arm of phase  $c$ ) and  $SW_4$  (a lower arm of phase  $b$ ) occur at  $t = 1$  s and  $t = 1.5$  s, respectively.

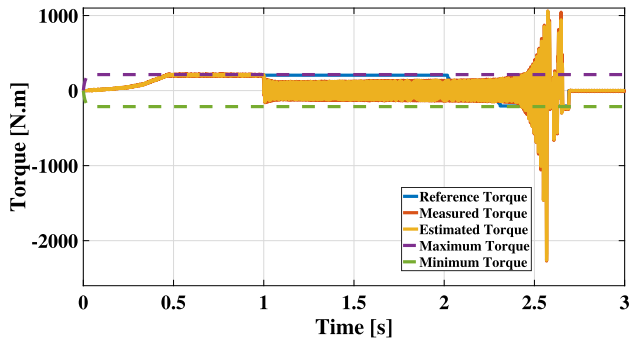


FIGURE 11. The PMSM reference, measured, estimated, maximum and minimum torques in case of an open-circuit fault in  $SW_1$ .

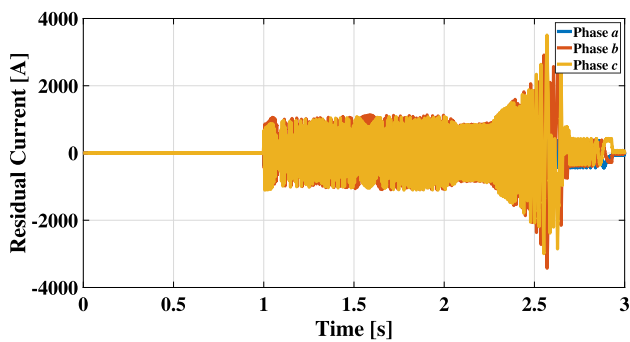


FIGURE 12. The three-phase residual current of the PMSM in case of an open-circuit fault in  $SW_1$ .

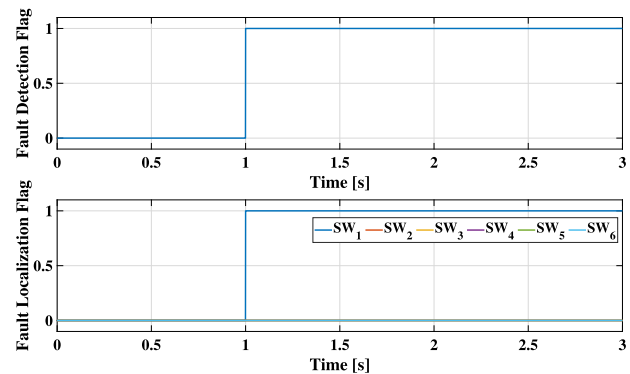


FIGURE 13. The diagnostic variables in case of an open-circuit fault in  $SW_1$ .

Such a faulty condition can be handled as two single switch faults. Based on Equation 25, the electrical torque is a function of the current in the  $q$ -axis. As shown in Figure 16, the three-phase residual current exceeds the predefined fault detection threshold. As a result of the open-circuit fault in  $SW_5$ ,  $i_q$  increases by 5%, and accordingly, the reference current changes. Additionally, due to the open-circuit fault in  $SW_4$ ,  $i_q$  changes by 20%. The notable squared Euclidean distance between the corresponding points in the collected dataset and the actual measurement leads to a successful localization of the two faulty switches. Figure 17 shows the diagnostic variables in case of open-circuit faults in  $SW_5$  and  $SW_4$ , in which the two faulty switches are successfully localized. Once the first two stages, i.e., open-circuit fault

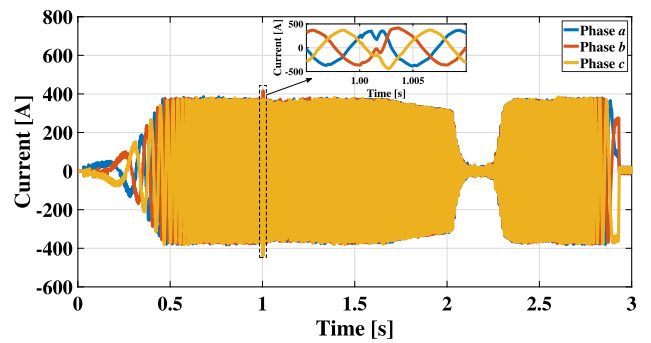


FIGURE 14. The three-phase current of the PMSM after clearing the open-circuit fault in  $SW_1$ .

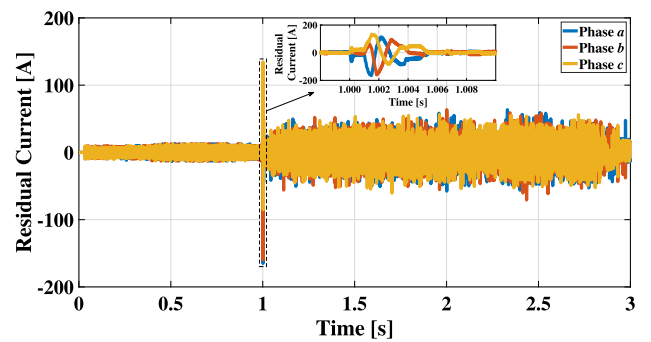


FIGURE 15. The three-phase residual current of the PMSM after clearing the open-circuit fault in  $SW_1$ .

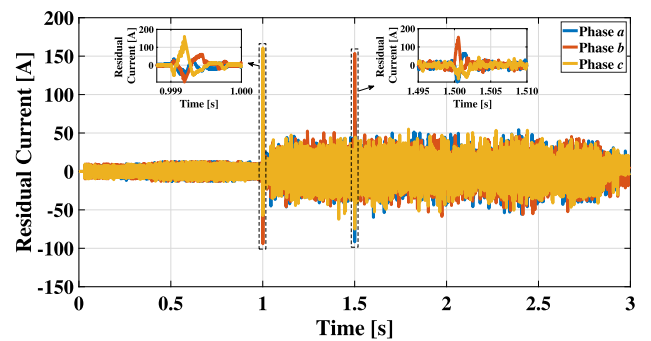


FIGURE 16. The three-phase residual current of the PMSM after clearing open-circuit faults in  $SW_5$  and  $SW_4$ .

detection and localization, are passed, the proposed method attempts to clear the two open-circuit faults by sending the closing commands to  $S_5$  and  $S_4$ , and as shown in Figure 18, the first and second faults are cleared within 1 ms. However, the first and second faults cause 3 kW and 2.5 kW changes in the mechanical power of the PMSM, respectively, using the proposed method causes efficient mitigation of such variations. In addition, no major impact on the DC-link voltage is observed. Since the stator voltage in the  $d$ -axis highly depends on the  $i_q$ , large variations are observed in  $v_d^*$ .

#### D. SIMULTANEOUS OPEN-CIRCUIT FAULTS IN SWITCHES

In the third scenario, it is assumed that simultaneous open-circuit faults occur in two switches  $SW_3$  and  $SW_6$  with a 0.5 ms time delay. Under such a faulty condition, the

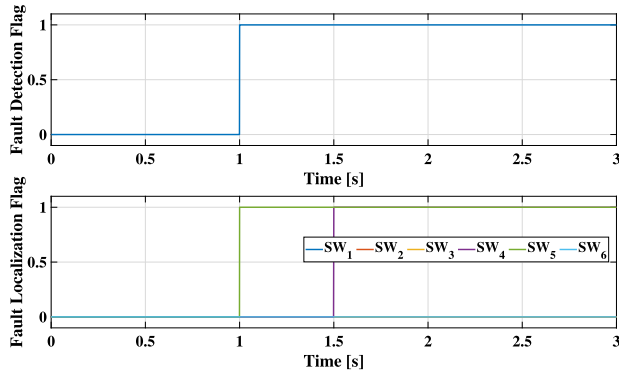


FIGURE 17. The diagnostic variables in case of open-circuit faults in  $SW_5$  and  $SW_4$ .

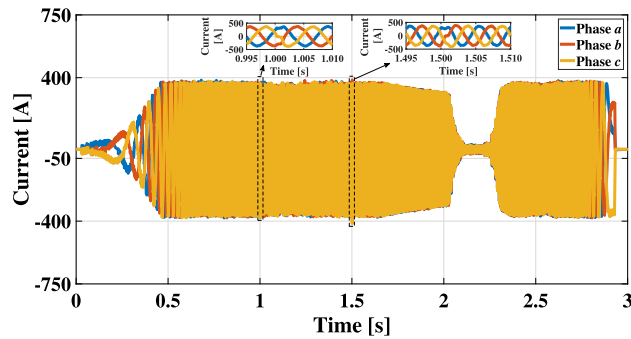


FIGURE 18. The three-phase current of the PMSM after clearing open-circuit faults in  $SW_5$  and  $SW_4$ .

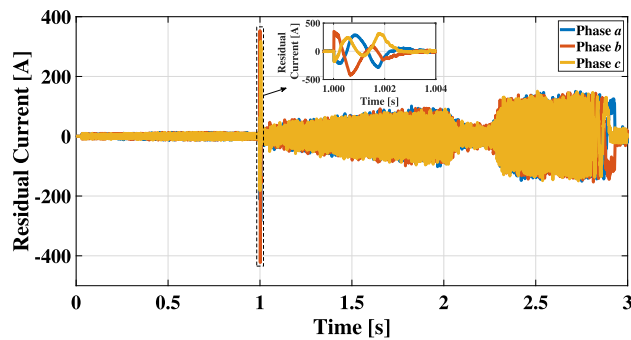


FIGURE 19. The three-phase residual current of the PMSM after clearing open-circuit faults in  $SW_3$  and  $SW_6$ .

VSI-fed PMSM drive system becomes fully unstable and uncontrollable. It is due to the fact that open-circuit faults in  $SW_3$  and  $SW_6$  directly impact the voltage of phases  $b$  and  $c$ , respectively, and since the coordination between the remaining switches is achieved, such faults cause a drastic increase ( $\times 100$ ) in the RoR of each phase current (except for the faulty arms), and obviously, this leads to severe damage to the entire electric drive-motor system. Hence, it is mandatory to clear such faults within a certain time period. In this case, simultaneous open-circuit faults in  $SW_3$  and  $SW_6$  respectively at  $t = 1$  s and  $t = 1.0005$  s (0.5 ms time delay) are investigated. Since simultaneous faults occur in the mentioned switches, as shown in Figure 19, the three-phase residual current evidently exceeds the predefined fault

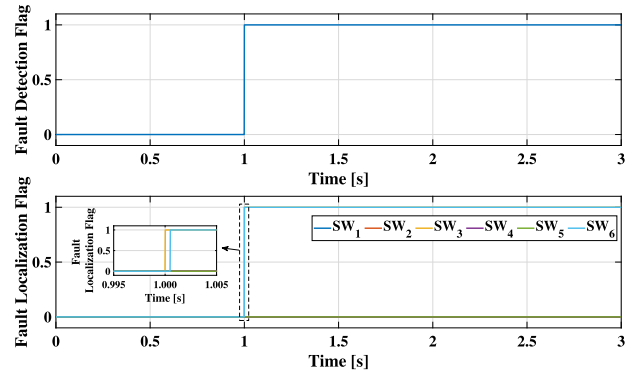


FIGURE 20. The diagnostic variables in case of open-circuit faults in  $SW_3$  and  $SW_6$ .

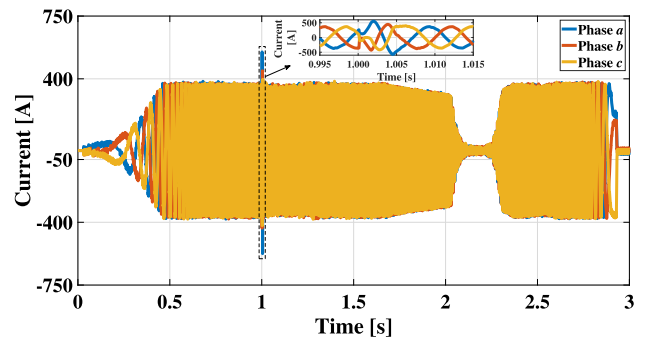


FIGURE 21. The three-phase current of the PMSM after clearing open-circuit faults in  $SW_3$  and  $SW_6$ .

detection threshold and this implies there is an open-circuit fault in the VSI-fed PMSM drive system.

In addition, such faults directly affect all three phases' current, and under such a faulty condition, the squared Euclidean distance between the actual measured phase current and the phase current under normal operating conditions exceeds the fault localization threshold, except for phases  $b$  and  $c$ . If no data-driven approach is implemented, the faulty switches can be localized using the output current waveform and by checking the switching patterns. Figure 20 shows the diagnostic variables in the case of open-circuit faults in  $SW_3$  and  $SW_6$ , in which the faulty condition and locations of the two faults are correctly determined. After successful detection and localization of the two faults, the faulty switches are bypassed by sending the closing commands to  $S_3$  and  $S_6$ , and the two faults are cleared. However, the proposed method attempts to clear the two faults, the three-phase residual current of the PMSM after clearing open-circuit faults in  $SW_3$  and  $SW_6$  is greater than normal operating conditions, which is indeed due to the difficult coordination between the remaining switches and newly connected ones. Figure 21 illustrates the three-phase current of the PMSM after clearing open-circuit faults in  $SW_3$  and  $SW_6$ . It should be mentioned that the scenario of simultaneous open-circuit faults in switches is a very rare case and the proposed method is capable of accurately and efficiently diagnosing such faults.

## V. CONCLUSION

In this paper, a fast online fault diagnosis approach for open-circuit faults in Insulated-Gate Bipolar Transistors (IGBTs) used in Voltage Source Inverter (VSI)-fed Permanent Magnet Synchronous Motor (PMSM) drive systems in Hybrid Electric Vehicles (HEVs) is proposed. Based on the provided results, the proposed three-stage combined model-based and data-driven fault diagnosis approach efficiently and accurately detects, locates, and clears open-circuit faults in IGBTs without the need for additional sensors. At the first stage of the proposed fault diagnosis approach, the three-phase voltage signals under normal operating conditions and various faulty conditions are analyzed, and the current in each phase using the normal operating conditions dataset is estimated to detect open-circuit faults. In the second stage, the Modified Multi-Class Support Vector Machine (MMC-SVM) algorithm with Radial Basis Function (RBF) kernel function, which is a data-driven approach, is applied to analyze the dataset collected under faulty conditions to locate such faults. Lastly, at the third stage, the proposed method bypasses such faults by sending the closing command to the corresponding backup switches and ensures the continuous operation of the VSI-fed PMSM drive system. The proposed method shows robustness against back-to-back and simultaneous open-circuit faults in IGBTs and does not rely on variations in the PMSM speed and power. The performance of the proposed fault diagnosis approach is evaluated using dynamic simulations in MATLAB. In addition, the obtained results show that the proposed method minimizes the computational burden to accurately diagnose the open-circuit faults in IGBTs and recovers the VSI-fed PMSM driver system to its normal operating conditions. Similar to HEVs, since Plug-in Hybrid Electric Vehicles (PHEVs) and Battery Electric Vehicles (BEVs) have an electric-drive motor system, the proposed method can be used to detect, locate, and clear open-circuit faults in IGBTs used in VSI-fed PMSM drive system in such vehicles.

## REFERENCES

- [1] F. Mohammadi, "Design, analysis, and electrification of a solar-powered electric vehicle," *J. Sol. Energy Res.*, vol. 3, no. 4, pp. 293–299, Dec. 2018.
- [2] F. Mohammadi, G.-A. Nazri, and M. Saif, "A bidirectional power charging control strategy for plug-in hybrid electric vehicles," *Sustainability*, vol. 11, no. 16, p. 4317, Aug. 2019.
- [3] C. Mehdipour, F. Mohammadi, and I. Mehdipour, "Analytical approach to nonlinear behavior study of an electric vehicle," in *Proc. 6th Int. Conf. Control, Instrum. Autom. (ICCIA)*, Oct. 2019, pp. 1–7.
- [4] F. Mohammadi, G.-A. Nazri, and M. Saif, "Modeling, simulation, and analysis of hybrid electric vehicle using MATLAB/simulink," in *Proc. Int. Conf. Power Gener. Syst. Renew. Energy Technol. (PGSRET)*, Aug. 2019, pp. 1–5.
- [5] F. Mohammadi and R. Rashidzadeh, "An overview of IoT-enabled monitoring and control systems for electric vehicles," *IEEE Instrum. Meas. Mag.*, vol. 24, no. 3, pp. 91–97, May 2021.
- [6] F. Mohammadi and M. Saif, "A comprehensive overview of electric vehicle batteries market," *e-Prime - Adv. Electr. Eng., Electron. Energy*, vol. 3, Mar. 2023, Art. no. 100127.
- [7] F. Mohammadi, M. Sanjari, and M. Saif, "A real-time blockchain-based state estimation system for battery energy storage systems," in *Proc. IEEE Kansas Power Energy Conf. (KPEC)*, Apr. 2022, pp. 1–4.
- [8] F. Mohammadi, "Lithium-ion battery state-of-charge estimation based on an improved Coulomb-counting algorithm and uncertainty evaluation," *J. Energy Storage*, vol. 48, Apr. 2022, Art. no. 104061.
- [9] B. Akin, S. Choi, and H. A. Toliyat, "DSP applications in electric and hybrid electric vehicles [in the spotlight]," *IEEE Signal Process. Mag.*, vol. 29, no. 3, pp. 133–136, May 2012.
- [10] S. A. Gadsden and S. R. Habibi, "Model-based fault detection of a battery system in a hybrid electric vehicle," in *Proc. IEEE Vehicle Power Propuls. Conf.*, Sep. 2011, pp. 1–6.
- [11] M. El Hachemi Benbouzid, "A review of induction motors signature analysis as a medium for faults detection," *IEEE Trans. Ind. Electron.*, vol. 47, no. 5, pp. 984–993, Oct. 2000.
- [12] S. Nandi, H. A. Toliyat, and X. Li, "Condition monitoring and fault diagnosis of electrical motors—A review," *IEEE Trans. Energy Convers.*, vol. 20, no. 4, pp. 719–729, Dec. 2005.
- [13] K.-T. Chau, "A software tool for learning the dynamic behavior of power electronics circuits," *IEEE Trans. Educ.*, vol. 39, no. 1, pp. 50–55, Feb. 1996.
- [14] M. A. Masrur, Z. Chen, and Y. Murphey, "Intelligent diagnosis of open and short circuit faults in electric drive inverters for real-time applications," *IET Power Electron.*, vol. 3, no. 2, p. 279, 2010.
- [15] B. Lu and S. K. Sharma, "A literature review of IGBT fault diagnostic and protection methods for power inverters," *IEEE Trans. Ind. Appl.*, vol. 45, no. 5, pp. 1770–1777, Sep. 2009.
- [16] J. O. Estima and A. J. M. Cardoso, "A new algorithm for real-time multiple open-circuit fault diagnosis in voltage-fed PWM motor drives by the reference current errors," *IEEE Trans. Ind. Electron.*, vol. 60, no. 8, pp. 3496–3505, Aug. 2013.
- [17] U.-M. Choi, F. Blaabjerg, and K.-B. Lee, "Reliability improvement of a T-type three-level inverter with fault-tolerant control strategy," *IEEE Trans. Power Electron.*, vol. 30, no. 5, pp. 2660–2673, May 2015.
- [18] U.-M. Choi, J.-S. Lee, F. Blaabjerg, and K.-B. Lee, "Open-circuit fault diagnosis and fault-tolerant control for a grid-connected NPC inverter," *IEEE Trans. Power Electron.*, vol. 31, no. 10, pp. 7234–7247, Oct. 2016.
- [19] D. Zhou, Y. Li, J. Zhao, F. Wu, and H. Luo, "An embedded closed-loop fault-tolerant control scheme for nonredundant VSI-fed induction motor drives," *IEEE Trans. Power Electron.*, vol. 32, no. 5, pp. 3731–3740, May 2017.
- [20] N. K. Nguyen, F. Meinguet, E. Semail, and X. Kestelyn, "Fault-tolerant operation of an open-end winding five-phase PMSM drive with short-circuit inverter fault," *IEEE Trans. Ind. Electron.*, vol. 63, no. 1, pp. 595–605, Jan. 2016.
- [21] R. R. Errabelli and P. Mutschler, "Fault-tolerant voltage source inverter for permanent magnet drives," *IEEE Trans. Power Electron.*, vol. 27, no. 2, pp. 500–508, Feb. 2012.
- [22] R. Peugot, S. Courtine, and J.-P. Rognon, "Fault detection and isolation on a PWM inverter by knowledge-based model," *IEEE Trans. Ind. Appl.*, vol. 34, no. 6, pp. 1318–1326, Nov. 1998.
- [23] A. M. S. Mendes and A. J. M. Cardoso, "Voltage source inverter fault diagnosis in variable speed AC drives by the average current Park's vector approach," in *Proc. IEEE Int. Electric Mach. Drives Conf. (IEMDC)*, May 1999, pp. 704–706.
- [24] W. Sleszynski, J. Nieznanski, and A. Cichowski, "Open-transistor fault diagnostics in voltage-source inverters by analyzing the load currents," *IEEE Trans. Ind. Electron.*, vol. 56, no. 11, pp. 4681–4688, Nov. 2009.
- [25] Z. Jian-Jian, C. Yong, C. Zhang-Yong, and Z. Anjian, "Open-switch fault diagnosis method in voltage-source inverters based on phase currents," *IEEE Access*, vol. 7, pp. 63619–63625, 2019.
- [26] C. Bae, D. Lee, and T. H. Nguyen, "Detection and identification of multiple IGBT open-circuit faults in PWM inverters for AC machine drives," *IET Power Electron.*, vol. 12, no. 4, pp. 923–931, Apr. 2019.
- [27] M. Saif, "Reduced order proportional integral observer with application," *J. Guid., Control, Dyn.*, vol. 16, no. 5, pp. 985–988, Sep. 1993.
- [28] B. Shafai and M. Saif, "Proportional-integral observer in robust control, fault detection, and decentralized control of dynamic systems," in *Control and Systems Engineering*. Cham, Switzerland: Springer, 2015.
- [29] D. R. Espinoza-Trejo, E. Bárcenas, F. J. Martínez-López, and D. U. Campos-Delgado, "Robust fault diagnosis scheme for open-circuit faults in voltage source inverters feeding induction motors by using non-linear proportional-integral observers," *IET Power Electron.*, vol. 5, no. 7, pp. 1204–1216, Aug. 2012.

- [30] D. R. Espinoza-Trejo, D. U. Campos-Delgado, G. Bossio, E. Bárcenas, J. E. Hernández-Díez, and L.F. Lugo-Cordero, "Fault diagnosis scheme for open-circuit faults in field-oriented control induction motor drives," *IET Power Electron.*, vol. 6, no. 5, pp. 869–877, May 2013.
- [31] Q.-T. An, L. Sun, and L.-Z. Sun, "Current residual vector-based open-switch fault diagnosis of inverters in PMSM drive systems," *IEEE Trans. Power Electron.*, vol. 30, no. 5, pp. 2814–2827, May 2015.
- [32] H. Yan, Y. Xu, J. Zou, Y. Fang, and F. Cai, "A novel open-circuit fault diagnosis method for voltage source inverters with a single current sensor," *IEEE Trans. Power Electron.*, vol. 33, no. 10, pp. 8775–8786, Oct. 2018.
- [33] F. Wu and J. Zhao, "A real-time multiple open-circuit fault diagnosis method in voltage-source-inverter fed vector controlled drives," *IEEE Trans. Power Electron.*, vol. 31, no. 2, pp. 1425–1437, Feb. 2016.
- [34] R. L. de Araujo Ribeiro, C. B. Jacobina, E. R. C. da Silva, and A. M. N. Lima, "Fault detection of open-switch damage in voltage-fed PWM motor drive systems," *IEEE Trans. Power Electron.*, vol. 18, no. 2, pp. 587–593, Mar. 2003.
- [35] S. Karimi, P. Poure, and S. Saadate, "Fast power switch failure detection for fault tolerant voltage source inverters using FPGA," *IET Power Electron.*, vol. 2, no. 4, pp. 346–354, Jul. 2009.
- [36] C. Choi and W. Lee, "Design and evaluation of voltage measurement-based sectoral diagnosis method for inverter open switch faults of permanent magnet synchronous motor drives," *IET Electr. Power Appl.*, vol. 6, no. 8, p. 526, 2012.
- [37] Q.-T. An, L.-Z. Sun, K. Zhao, and L. Sun, "Switching function model-based fast-diagnostic method of open-switch faults in inverters without sensors," *IEEE Trans. Power Electron.*, vol. 26, no. 1, pp. 119–126, Jan. 2011.
- [38] S.-M. Jung, J.-S. Park, H.-W. Kim, K.-Y. Cho, and M.-J. Youn, "An MRAS-based diagnosis of open-circuit fault in PWM voltage-source inverters for PM synchronous motor drive systems," *IEEE Trans. Power Electron.*, vol. 28, no. 5, pp. 2514–2526, May 2013.
- [39] S. Khomfoi and L. M. Tolbert, "Fault diagnostic system for a multilevel inverter using a neural network," *IEEE Trans. Power Electron.*, vol. 22, no. 3, pp. 1062–1069, May 2007.
- [40] P. Sobanski and M. Kaminski, "Application of artificial neural networks for transistor open-circuit fault diagnosis in three-phase rectifiers," *IET Power Electron.*, vol. 12, no. 9, pp. 2189–2200, Aug. 2019.
- [41] S. S. Moosavi, A. Djerdir, Y. Ait-Amirat, D. A. Khaburi, and A. N'Diaye, "Artificial neural network-based fault diagnosis in the AC–DC converter of the power supply of series hybrid electric vehicle," *IET Electr. Syst. Transp.*, vol. 6, no. 2, pp. 96–106, Jun. 2016.
- [42] B. Cai, Y. Zhao, H. Liu, and M. Xie, "A data-driven fault diagnosis methodology in three-phase inverters for PMSM drive systems," *IEEE Trans. Power Electron.*, vol. 32, no. 7, pp. 5590–5600, Jul. 2017.
- [43] F. Zidani, D. Diallo, M. E. H. Benbouzid, and R. Nait-Said, "A fuzzy-based approach for the diagnosis of fault modes in a voltage-fed PWM inverter induction motor drive," *IEEE Trans. Ind. Electron.*, vol. 55, no. 2, pp. 586–593, Feb. 2008.
- [44] H. Yan, Y. Xu, F. Cai, H. Zhang, W. Zhao, and C. Gerada, "PWM-VSI fault diagnosis for a PMSM drive based on the fuzzy logic approach," *IEEE Trans. Power Electron.*, vol. 34, no. 1, pp. 759–768, Jan. 2019.
- [45] S. Moosavi, H. Akbari, and S. Valipour, "An open-circuit fault detection method with wavelet transform in IGBT-based DC/AC inverter used in electric vehicles," *Int. J. Power Electron. Drive Syst. (IJPEDS)*, vol. 9, no. 3, p. 1240, Sep. 2018.
- [46] Z.-K. Hu, W.-H. Gui, C.-H. Yang, P.-C. Deng, and S. X. Ding, "Fault classification method for inverter based on hybrid support vector machines and wavelet analysis," *Int. J. Control, Autom. Syst.*, vol. 9, no. 4, pp. 797–804, Aug. 2011.
- [47] C. Bowen and T. Wei, "Switch open-circuit faults diagnosis of inverter based on wavelet and support vector machine," in *Proc. 14th IEEE Int. Conf. Electron. Meas. Instrum. (ICEMI)*, Nov. 2019, pp. 1178–1184.
- [48] F. Mohammadi and C. Zheng, "A precise SVM classification model for predictions with missing data," in *Proc. Nat. Conf. Appl. Res. Electr., Mech. Comput. IT Eng.*, Oct. 2018, pp. 1–5.
- [49] F. Mohammadi, G.-A. Nazri, and M. Saif, "A fast fault detection and identification approach in power distribution systems," in *Proc. Int. Conf. Power Gener. Syst. Renew. Energy Technol. (PGSRET)*, Aug. 2019, pp. 1–4.
- [50] F. Mohammadi, M. Mirhashemi, and R. Rashidzadeh, "A coordinate measuring machine with auto-learning capability," in *Proc. 2nd Int. Conf. Electr., Control Instrum. Eng. (ICECIE)*, Nov. 2020, pp. 1–8.
- [51] F. Mohammadi, M. Mirhashemi, and R. Rashidzadeh, "A coordinate measuring machine with error compensation in feature measurement: Model development and experimental verification," *Int. J. Adv. Manuf. Technol.*, Jan. 2022. [Online]. Available: <https://link.springer.com/article/10.1007/s00170-021-08362-y>

•••